Measurements of Muon and Muon-induced Fluxes Using Gadolinium-Doped Liquid Scintillator at the China Jinping Underground Laboratory

Authors: Peng, Mr. Xiaoyu, Fang, Mr. Changhao, Lin, Mr. Shin-Ted, Liu, Prof. Shukui, Li, Mr. Hanyu, Li, Miss Qianyun, LiRen, Mr. Mingjie, Liu, Dr. Yu, Shi, Mr. Haoyu, Wang Qin, Please provide the Chinese academic text to be translated., Yan, Dr. Yulu, Yang, Dr. Litao, Yue, Prof. Qian, Zhu, Mr. J.J., Lin, Mr. Shin-Ted

Date: 2025-06-05T22:49:41+00:00

Abstract

We present the results of an experiment conducted to measure cosmic-ray muons and muon-induced fluxes at the China Jinping Underground Laboratory. Utilizing a 28-liter 0.5% gadolinium-doped liquid scintillator detector, which operated stably for 412 days in a 1-meter-thick polyethylene shielding, we reconstructed saturated signal pulses and pulse shape discrimination to facilitate measurements across a range starting from 0.2 MeV. The event rates incorporating mountain geometry effects for cosmic rays and their induced particles are derived. The experimental results show that cosmic ray muon flux is (3.64 ± 0.69(stat.) ± 0.25(syst.)) × 10^{-10} cm^{-2} s^{-1}, muon-induced electron flux is (5.59 ± 1.06(stat.) ± 0.40(syst.)) × 10^{-10} cm^{-2} s^{-1}, and the upper limit of the muon-induced neutron flux is 3.52 × 10^{-9} cm^{-2} s^{-1}. They indicated that no significant excess is observed at a 90% confidence-level, particularly no muon-induced neutrons above 10 MeVee is detected.

Full Text

Measurements of Muon and Muon-induced Fluxes Using Gadolinium-Doped Liquid Scintillator at the China Jinping Underground Laboratory

Xiao-Yu Peng,[1] Chang-Hao Fang,[1] Shin-Ted Lin,[1],† Shu-Kui Liu,[1],‡ Han-Yu Li,[1] Qian-Yun Li,[1] Ren-Ming-Jie Li,[1] Yu Liu,[1] Hao-Yu Shi,[1]

Qin Wang,[1] Hao-Yang Xing,[1] Yu-Lu Yan,[1] Li-Tao Yang,[2] Qian Yue,[2] and Jing-Jun Zhu[1]

[1]College of Physics, Sichuan University, 610065 Chengdu, China
[2]Key Laboratory of Particle and Radiation Imaging (Ministry of Education) and Department of Engineering Physics, Tsinghua University, 100084 Beijing, China

Abstract

We present results from an experiment measuring cosmic-ray muons and muon-induced fluxes at the China Jinping Underground Laboratory. Using a 28-liter gadolinium-doped liquid scintillator detector (0.5% Gd concentration) that operated stably for 412 days inside a 1-meter-thick polyethylene shielding, we reconstructed saturated signal pulses using pulse shape discrimination to enable measurements down to 0.2 MeV. The event rates incorporating mountain geometry effects for cosmic rays and their induced particles are derived. The experimental results show that the cosmic-ray muon flux is (3.64 ± 0.69_stat $\pm$ 0.25_syst) $\times$ 10^{1} cm^{2} s^{1}, the muon-induced electron flux is (5.59 ± 1.06_stat $\pm$ 0.40_syst) $\times$ 10^{1} cm^{2} s^{1}, and the upper limit of the muon-induced neutron flux is 3.52×10 cm^{2} s^{1}. These results indicate no significant excess at 90% confidence level, particularly with no muon-induced neutrons above 10 MeVee detected.

Keywords: Neutron detector, Cosmic ray, Muon flux, Saturated signals, Signal reconstruction

INTRODUCTION

Cosmic-ray muons constitute a major background in rare-event detection experiments targeting dark matter particles [1–3], neutrinoless double-beta decay [4,5], and neutrino property studies [6]. The high penetration power of muons enables them to traverse multi-kilometer-thick rock overburdens and directly interact with detectors, contaminating rare-event signals [7]. High-energy muons also generate secondary particles through interactions with materials, producing muon-induced neutrons and electrons. Muon-induced neutrons present particularly severe challenges: in low-energy regimes, neutron signals become indistinguishable from Weakly Interacting Massive Particle (WIMP)-nucleon collisions [8]; neutron inelastic scattering produces gamma backgrounds that mask neutrinoless double-beta decay events; and neutron elastic scattering signals overlap with neutrino interactions [9]. Consequently, rare-event experiments are predominantly deployed in underground laboratories, where multi-kilometer-thick rock layers effectively shield cosmic-ray muons.

The world's underground laboratories with depths exceeding 2000 meters include the China Jinping Underground Laboratory (CJPL) (2400 meters) [10,11] and Canada' s Sudbury Neutrino Observatory (SNO) (2000 meters) [12], where the cosmic-ray muon flux is as low as 10^{1} cm^{2} s^{1}. Located in the Jinping Tunnel in Sichuan Province, China, CJPL is currently the deepest underground laboratory

in the world, with over 1,500 meters of rock covering the facility and a maximum vertical rock depth of up to 2,400 meters [10]. The thick rock surrounding the laboratory creates an environment with an exceptionally low background level throughout the facility. Nevertheless, backgrounds from cosmic-ray muons and muon-induced neutrons remain non-negligible, making it essential to measure their flux at CJPL.

For cosmic-ray muons, Wu et al. used a plastic scintillator telescope to measure muons in the vertical direction, obtaining an initial cosmic-ray flux of (2.0 ± 0.4) × 10 ¹ cm ² s ¹ without applying angular corrections [13]. Guo et al. carefully considered the geometric structure of the mountain and corrected for the detector' s acceptance angle, thereby obtaining a more accurate measurement of the cosmic-ray flux: (3.53 ± 0.22_stat ± 0.07_syst) × 10 ¹ cm ² s ¹ [14].

The flux of muon-induced neutrons is typically one order of magnitude lower than that of cosmic-ray muons [15]. For neutron detection, a 0.5% gadolinium-doped liquid scintillator (Gd-LS) detector has been developed. Previous experiments have demonstrated that the Gd-LS detector exhibits excellent n- discrimination and neutron detection capabilities [16–20], achieved through pulse shape discrimination (PSD). The underlying mechanism relies on distinct energy deposition patterns: neutron-induced nuclear recoils produce signals with longer decay tails compared to gamma-induced electronic recoils, enabling discrimination via an integral-dependent discrimination factor (Dis factor). Neutron detection is accomplished by analyzing the fast signal (generated by elastic scattering of neutrons with nuclei), the slow signal (resulting from neutron capture on gadolinium), and the time interval between them. Specifically, neutrons entering the Gd-LS detector produce fast signals through elastic scattering with nuclei. As neutrons slow down and lose energy, they may be captured by gadolinium nuclei, emitting gamma rays with energies around 8 MeV, which generate the slow signals. To reject background events caused by gamma radiation, a neutron event is validated only if the time interval between the fast and slow signals exceeds 2 μs and is less than 40 μs.

Additionally, neutrons originating from environmental (, n) reactions and spontaneous fission induced by U/Th decay must be distinguished from muon-induced neutrons [21–29]. Environmental neutrons predominantly arise from the rock surrounding the laboratory and the detector materials, with energies typically below 10 MeV [30–32]. To shield against rock-origin neutrons, a 1-meter-thick polyethylene (PE) room has been constructed. Utilizing the Gd-LS detector and PSD method, Du et al. obtained neutron energy spectrum measurements in the 1 to 10 MeV range within the CJPL Phase I laboratory hall and the PE room [16]. These measurements were conducted using the SAND-II algorithm to unfold the neutron spectrum. The results indicated that the neutron flux in the CJPL Phase I laboratory hall was (1.51 ± 0.03_stat ± 0.1_syst) × 10 cm ² s ¹, while in the PE room it was (4.9 ± 0.9_stat ± 0.5_syst) × 10 cm ² s ¹. These measurements provide valuable assessments of neutrons in the laboratory, facilitating the application of the Gd-LS detector for

ultra-low flux measurements (10^{-11} cm^{-2} s^{-1}). To obtain the source of neutron background in the PE room, Zhong et al. employed a genetic algorithm to optimize the energy spectral continuum, thereby enabling the identification of the U-Th content in the material and determining the source and yield of the primary neutrons [19,33]. The results indicated that 92.5% of the neutrons in the PE room originated from the aluminum protection plates near the detector, which were found to have a high thorium contamination of (1421.6 ± 171.1) μg/kg.

Muon, muon-induced electrons, and muon-induced neutrons exhibit higher energies than environmental background [34–36]. This energy difference allows an energy threshold (above 10 MeV) to effectively distinguish muon and muon-induced events from environmental backgrounds. To differentiate particle types, this study employs the PSD method. However, a critical limitation arises from the Data Acquisition (DAQ) system' s dynamic range: high-energy interactions with the scintillator produce saturated output signals exceeding the DAQ' s measurement range. Signal saturation introduces nonlinearities and waveform information loss, necessitating saturated signal reconstruction to enable accurate measurements of cosmic-ray muon flux, muon-induced neutron flux, and muon-induced electron flux in the high-energy regime.

In this study, a compact Gd-LS detector (28 L liquid scintillator) and function-fitting method are utilized to conduct full-directional measurements of cosmic muon flux, muon-induced electron flux, and muon-induced neutron flux in the PE room of the CJPL. This study demonstrates the feasibility of employing miniaturized detectors for precise quantification of ultra-low-flux experimental backgrounds (10^{-1} cm^{-2} s^{-1}). Section II details the experimental configuration of the detector and its data acquisition system. Section III describes the saturation signal reconstruction algorithm based on function-fitting techniques. Section IV outlines the Geant4 simulation framework [37] for detector efficiency calibration and the methodology for determining muon flux, muon-induced electron flux, and muon-induced neutron flux. Finally, Section V discusses the results and prospects for future applications in underground rare-event experiments.

28-LITER GADOLINIUM-DOPED LIQUID SCINTILLATOR DETECTOR

The Gd-LS detector, located in the CJPL PE room, is a cylindrical detector with a diameter of 0.3 m and a length of 0.4 m. It is filled with 28 liters of EJ-335 liquid scintillator contained in a quartz glass vessel with a thickness of only 4 mm. The scintillator is doped with 0.5% of the total mass of gadolinium. For EJ-335, the density is 0.89 g/cm^3, and its scintillation light output is as reported in [38]. The scintillation light attenuation length is 4.5 m (applicable to large-volume detectors). The quartz glass vessel is coated with a polytetrafluoroethylene (PTFE) reflective layer on its sides to enhance photon collection efficiency. Hamamatsu R5912-02 photomultiplier tubes (PMTs) are attached to both ends of the vessel, providing double-ended readout for signal collection.

Additionally, lead plates, aluminum plates, and PE block shields surround the detector, and the entire experimental setup is positioned in one corner of the PE room.

DATA ACQUISITION SYSTEM

The schematic diagram of the DAQ system is shown in Fig. 1. Signals from two PMTs and a high-precision pulse generator are split into two channels using three Fan-In/Fan-Out (FIFO) units. One channel is directly input into a Flash Analog-to-Digital Converter (FADC) module operating at a sampling rate of 500 MHz with 8-bit resolution. The other channel is directed to three discriminators: signals from the two PMTs pass through discriminators and are processed by a logical AND unit to generate a coincidence signal, while the pulse generator signal is processed by a discriminator and combined with the PMT coincidence signal via a logical OR unit. The output of the logical OR unit serves as the FADC trigger signal. When both PMTs simultaneously detect signals exceeding the threshold or the pulse generator emits a pulse, the FADC initiates waveform sampling. Digitized waveforms are transmitted via optical fiber and stored on a computer. Fixed-frequency pulse signals from the generator are used to calculate dead time and data selection efficiency.

Environmental neutrons and gamma rays typically exhibit energies below 10 MeV [39], and their full signals are measurable by the Gd-LS detector. Surviving cosmic-ray muons, with an average energy of 340 GeV, generate extremely large signals when detected alongside their secondary particles. Due to DAQ system parameter constraints, the maximum amplitude of recorded waveforms (excluding baseline) is limited to 244.5 ADC units. Signals exceeding this threshold are truncated. Prior studies confirm that events below 10 MeV are recorded successfully [16], whereas events above 10 MeV predominantly exhibit saturation. To reconstruct saturated events, a function-fitting method is applied. An artificial neural network (ANN) reconstruction is also implemented, with results demonstrating satisfactory accuracy.

This study analyzes data collected during 412 days of stable detector operation. The dataset includes all signals unambiguously distinguishable from noise, with stable trigger rates, baselines, and baseline fluctuations.

SATURATION SIGNAL RECONSTRUCTION

Function-Fitting Method

Saturation-induced signal truncation caused by the dynamic range limitation of the DAQ system leads to irreversible loss of complete waveform morphology and charge integral data. Since the charge integral is a critical parameter directly proportional to energy deposition and the Dis factor of detection events, precise reconstruction of saturated signals becomes essential for comprehensive waveform recovery. The hypothesis posits that signal waveforms with differ-

ent amplitudes exhibit analogous shape characteristics. To test this hypothesis, an artificial neural network (ANN) methodology is employed [40]. This study utilizes a generalized radial basis function (GRBF) neural network, a topology validated for robust signal reconstruction performance [40,41].

Four amplitude ranges are designated as training cohorts: 50–100, 100–150, 150–200, and 200–saturation (244.5 ADC units), with training sets containing 10,000, 10,000, 10,000, and 88 events, respectively. The scarcity of signals in the 200–244.5 range arises from the limited number of high-energy gamma-ray events emitted after neutron capture by gadolinium nuclei. All training samples are randomly selected from detection datasets to ensure statistical representativeness, with reduced population in the final cohort reflecting natural amplitude distribution sparsity. The top panel of Fig. 2 displays ANN outputs as characteristic scatter distributions: black inverted triangles (50–100), pink squares (100–150), purple circles (150–200), and blue pentagrams (200–saturation). These clustered distributions validate the waveform similarity hypothesis across amplitude ranges.

Parallel reconstruction efforts apply a function-fitting method to saturated signals. Red curves in Fig. 2 (top) represent fits to all ANN output points using Equation (1), where p , p , and p denote peak amplitude, peak time, and half-height width, respectively. Table 1 compares ANN and function-fitting reconstruction results, showing integration average deviation within a few thousandths across all amplitude ranges. The bottom panel of Fig. 2 demonstrates the reconstruction of a saturated signal: black scatters represent raw data, the red curve is the fitted function, and 244.5 ADC units mark the DAQ dynamic range limit. Both panels in Fig. 2 confirm the function' s ability to approximate waveform morphology. However, the function aligns closely with low-amplitude waveforms but deviates slightly at higher amplitudes.

Analysis of Bias Values

To quantify systematic deviations introduced by the fitting function during waveform reconstruction, we define two distinct bias categories for systematic error characterization. This analysis specifically focuses on the reconstructed charge integral bias of physical events, calculated through statistical averaging over multiple events processed by the fitting procedure. Parameter estimation errors from the fitting process are not analyzed independently, as these errors are inherently embedded within the statistical ensemble treatment and thus contribute intrinsically to the observed charge integral bias.

The first type of bias arises from imperfect alignment between Eq. (1) and the actual waveform, leading to systematic deviations when fitting high-amplitude waveforms. The analysis framework employs unsaturated signals as baseline references across four amplitude ranges: 50–100, 100–150, 150–200, and 200–saturation (244.5 ADC units). Quantitative evaluation of charge integral bias magnitudes within these ranges enables systematic uncertainty estimation for

saturated signals caused by waveform truncation due to information loss. Larger saturated signal amplitudes result in more severe truncation, exacerbating information loss and thereby increasing reconstruction bias. Eq. (2) is defined to characterize this first bias type:

$$\text{Bias} = \frac{Q_f - Q_r}{Q_r}$$

where Q_f is the integral under the model of the fitting function and Q_r is the area integral of the real waveform. Bias denotes the degree of bias of the modeled integral of the fitted function from the actual integral of the real waveform.

Fig. 3(a) displays amplitude-dependent bias distributions via color-coded histograms for the four amplitude ranges. The lower inset shows expectation values and standard deviations derived from Gaussian fits. As shown in Fig. 3(a), waveform integral biases using Eq. (1) remain below 0.006 (0.6%), with decreasing trends as amplitudes increase. For the highest amplitude range (200–saturation), the bias measures 0.0023 and follows this decreasing pattern. This confirms the first-type bias for saturated signal reconstruction using Eq. (1) is bounded at 0.0023. Systematic analysis thereby validates that first-type biases remain within acceptable thresholds for practical applications, justifying their exclusion in subsequent analyses.

The second type of bias stems from reconstruction errors in truncated waveforms. To quantify this, an Artificial Cut (AC) is applied to waveforms within the 100–150 amplitude range. The AC mimics truncation-induced information loss analogous to natural Cut. This amplitude range provides sufficient event statistics (10,000 events per Cut value from 10% to 80%) to reliably characterize potential truncation levels in saturated signals. Integral bias is calculated similarly to the first bias type, with results shown in Fig. 3(b). Prior to analyzing this bias, the Cut parameter is defined to quantify the truncation extent using Eq. (3):

$$\text{Cut} = \frac{A - 244.5}{A} \times 100\%$$

where 244.5 ADC units denotes the DAQ dynamic range limit, and A represents the fitted peak amplitude. A higher Cut value indicates greater waveform truncation, while a lower Cut corresponds to minimal truncation.

Fig. 3(b) displays integral bias distributions for varying Cut values via color-coded histograms, with red dashed lines denoting Gaussian fits. The lower inset presents Gaussian-fitted mean values. Results demonstrate that higher Cut values yield larger biases and broader distributions, validating the hypothesis that reconstructing heavily truncated waveforms introduces greater deviations. For 80% Cut, the bias reaches 10.7%, whereas 10% Cut results in 0.2% bias. This confirms that the reconstruction function significantly impacts waveform

fidelity, necessitating bias correction in both energy and Dis factor calculations for saturated signals.

Results of Reconstruction

Following the evaluation of reconstruction biases, saturated signal events are reconstructed. The correction factor (CF) is defined as CF = 1 - bias, where bias quantifies the systematic deviations described in the previous section. The reconstructed charge integral is calculated using Eq. (4), which incorporates CF to correct for bias effects:

$$Q = \mathrm{CF} \times Q_f$$

The Gd-LS detector employs a dual PMT readout system, with PMTs positioned at the front and back ends to collect light signals. Consequently, each event generates two distinct waveforms. The total charge integral Q_total is defined as the geometric mean of the charge integrals from both PMTs (Q and Q), expressed in Eq. (5):

$$Q_{\mathrm{total}} = \sqrt{Q_1 \times Q_2}$$

The Dis factor is computed via Equation (6), where Q _part and Q _part represent the charge integrals within a 15 ns window following the signal peak (see Fig. 2, bottom). Error propagation methods are applied to estimate uncertainties in Q_total and Dis factor, accounting for statistical variances in Q _part, Q _part, and temporal measurements.

$$\mathrm{Dis} = \frac{Q_{1\ \mathrm{part}} + Q_{2\ \mathrm{part}}}{Q_1 + Q_2}$$

Fig. 4 presents the reconstruction results of saturated events. The left panel shows a two-dimensional scatter plot of Q-value versus Dis for reconstructed events, with all Dis values strictly below 0.15, aligning with the waveform morphology of gamma events. The Q-values cluster around 10,000, indicating these saturated events likely originate from cosmic-ray muons traversing the detector. The right panel presents a similar Q-Dis scatter plot including low-energy background signals, where the red curve marks the gamma-like event trend. This distribution confirms the classification of reconstructed saturated events as gamma-like signals induced by cosmic-ray muon interactions. Consequently, the 26 reconstruction events are designated as muon event candidates.

Event Selection

Based on the detector geometry, cosmic-ray muons deposit approximately 50 MeV of energy over a mean trajectory length of 30 cm within the detector.

To suppress background contamination from environmental gamma events and peripheral muon interactions, muon candidates are selected with energy thresholds exceeding 10 MeV. Under this selection criterion, PMT flasher events and electronic noise become dominant background sources in the high-energy region. PMT flasher events originate from spontaneous light emission caused by base discharge within PMTs, whereas electronic noise stems from baseline fluctuations in the readout electronics induced by external interference. Both background types exhibit anomalously high waveform amplitudes localized to specific PMT channels. To discriminate these backgrounds from genuine muon signals, a parameter r related to waveform amplitude is defined, which equals the ratio of the difference between the right and left waveform amplitudes to their sum ($|(R - L)/(R + L)|$), where L and R denote the signal amplitudes from the left and right PMTs, respectively.

We compare reconstructed events with a large sample of pre-identified low-energy gamma events. These gamma events originate from neutron capture by gadolinium nuclei, emitting characteristic gamma rays. Characterized by low energy (typically below 5 MeV) and selected via time correlation criteria, these events are uncontaminated by PMT flasher artifacts or electronic noise. Fig. 5 compares the amplitude asymmetry parameter r between low-energy gamma events and reconstructed events. The left panel shows r distribution, revealing a higher density of saturated events in the 0.2–0.4 range. The right panel displays a two-dimensional Q-value versus r scatter plot, with saturated event Q-values scaled by 0.1 for visual contrast. The five lowest-energy reconstructed events consistently lie outside the candidate region, classifying them as background. Furthermore, all saturated events exhibited large waveform amplitudes (with the smallest being approximately 244.5 ADC units), and the probability of simultaneous flasher event occurrence in the dual-PMT system is extremely low. Therefore, we attribute these background events to electronic noise. After stringent selection, 21 events remain as validated muon candidates.

GEANT4 SIMULATIONS

To calculate the detector's active area, investigate potential neutron background contributions, determine neutron detection efficiency, calibrate the high-energy response of the detector system, and estimate the fluxes of muons, muon-induced electrons, and muon-induced neutrons, we performed Monte Carlo simulations using Geant4 software (version 4.10.06).

Simulation Settings

In the particle source configuration, the GeneralParticleSource in Geant4 is used to generate cosmic-ray muons, with the cosmic-ray muon energy and incidence angle inputs derived from measurements conducted at the CJPL by Guo et al. [14]. The total muon flux is 3.53×10^{-1} cm^{-2} s^{-1} with an average energy of 340 GeV. The distributions of muon energy, azimuthal and zenithal angles are illustrated schematically in Fig. 6(a), (b) and (c). In addition, the impact of the

mountainous structure above the laboratory on the muons has been taken into account through recent measurement. Based on this consideration, there are more muon events originating from the southwest and southeast directions. The location of the particle source is illustrated in Fig. 6(d). Muons are generated in a circular plane 5 meters directly above the detector, with a radius of 5 meters.

In the detector geometry configuration, the detector model is illustrated in Fig. 6(d). A PE room with dimensions 8 m (length) × 5.6 m (width) × 4.1 m (height) is simulated using 1 m thick PE sheets (green squares). The detector is positioned in one corner of the PE room, fully enclosed by the PE sheets. A 0.6 m × 0.6 m × 0.05 m lead plate (pink square) is installed at the front of the detector, while 0.005 m thick aluminum plates (yellow squares) shield the rear and sides. The detector body comprises a cylindrical structure with a diameter of 0.3 m and length of 0.4 m (brown cylinder), surrounded by a PTFE reflective layer (gray cylinder). In the experimental setup, glass light guides and PMTs are mounted on both ends of the detector body.

Detector Active Area

The detector' s active area is estimated by analyzing simulated muon events. An exposure unit is defined as 412 days of continuous detector operation, equivalent to 9,685 muons traversing a circular region with a 5-meter radius above the detector. Through 3,000 simulated exposure units, the event count distribution shown in Fig. 7 yields a mean of 19.2 events per exposure unit. From this result, the mean event count is calculated as N_μ = 19.2. The active area S is calculated using:

$$S = \frac{N}{T \times \phi_{\text{sim}}}$$

where S represents the detector' s active area, T denotes the operational live time (412 days in this experiment, or 3.56 × 10 s), and _sim corresponds to the simulated muon flux (3.53 × 10 ^{1} cm ^{2} s ^{1}). The calculated active area is S = 1528 cm².

Energy Deposition Spectrum and Muon-Induced Neutron Sources

To estimate the composition of the reconstructed energy spectrum, correct the detector's energy response, and investigate potential neutron background contributions, simulations are conducted with muon events equivalent to 1,000 times the experimental exposure. The simulation results are shown in Fig. 8. The upper panel displays the electron-equivalent energy (MeVee) spectrum below 100 MeVee in the detector, normalized to events per day per MeVee. This spectrum demonstrates that muon events dominate visible events above 10 MeVee. In the 10–20 MeVee range, a small fraction of muon-induced electron events contributes to the spectrum. Additionally, recoil protons produced by elastic scattering between muon-induced neutrons and hydrogen nuclei generate visible

energy after quenching effects. As shown by the pink band in the upper panel, muon-induced neutron events are approximately two orders of magnitude less frequent than muon events, with most exhibiting energies below 5 MeVee.

The lower panel of Fig. 8 illustrates the spatial distribution of muon-induced neutron production within the PE room under these simulation conditions. The results reveal that while most neutrons originate from interactions at the PE room walls, detectable neutron-induced events primarily occur inside the detector. This spatial discrepancy arises because the 1-meter-thick polyethylene shielding effectively attenuates external neutrons, whereas internal neutron events result from muons directly penetrating the detector.

Muon-Induced Neutron Detection Efficiency

The neutron detection efficiency is defined as the ratio of neutrons undergoing reactions in the LS to the total neutrons entering the detector, expressed as:

$$\epsilon_d = \frac{N_1}{N_{\text{Total}}}$$

where N represents the number of neutrons that undergo elastic scattering with hydrogen nuclei in LS, and N_Total is the total neutrons entering the detector. These values are derived from simulations. With 10,000 muon-induced neutrons generated (sampled according to the neutron energy spectrum), 5,312 events satisfied the selection criteria. The efficiency is thus calculated as _d = 53.1%.

Additionally, the geometric efficiency _g is defined as the ratio of neutrons entering from outside the detector's sensitive volume to the total neutrons. This definition accounts for the fact that only external neutrons can be effectively detected, as internal neutrons produced by muons traversing the detector are obscured by higher-amplitude muon signals and cannot be distinguished. The lower inset of Fig. 8 illustrates the simulated distribution of muon-induced neutrons, showing that external neutrons constitute 20% of the visible neutron population. Therefore, _g = 20%.

Correction of Detector Energy Response

When a Hamamatsu R5912-02 PMT receives a large number of photons, the anode output current increases sharply. In the region of the last dynode, electron accumulation forms a space charge, generating a reverse electric field that weakens the accelerating field strength and reduces secondary electron emission efficiency. Consequently, the detector exhibits non-linear energy responses above 10 MeV. Correcting this non-linearity is essential to reconstruct the true energy of events accurately.

The energy response below 10 MeV is calibrated using gamma sources Co and ^{13} Cs. For energies above 10 MeV, calibration is achieved by comparing the Q-values of reconstructed saturated events with simulated muon energy deposition

peaks. These three calibration points are shown in the upper inset of Fig. 9. The small inset within the upper panel provides a magnified view of the low-energy region, where red and green lines represent cubic polynomial and linear fits, respectively. The error of the calibration point is determined by the error of the mean value obtained from a Gaussian fit to the simulated peak and the uncertainty of the peak position of integral spectrum. The minimal discrepancy between the two fits below 10 MeV, deviating by only a few percent near 10 MeV, justifies approximating the response as linear in this range. The lower inset of Fig. 9 displays the reconstructed energy of muon candidate events using the corrected energy response curve.

RESULTS

Systematic Uncertainties

Table 2 summarizes the total systematic uncertainties. The dominant systematic uncertainties arise from the reconstructed energy, the energy scale, the radius of the quartz glass vessel, the wall thickness of the PE room, the PE shielding layer, and the Pb shielding layer.

The uncertainty in the energy scale originates from the uncertainty in the calibration points, which comes from two aspects: the mean value error obtained through Gaussian fitting of the simulated energy spectrum peak and the uncertainty of the peak position of integral spectrum. The uncertainty of the peak position in the integral spectrum is given by the difference between the distribution of the upper and lower errors in the reconstructed integral. Consequently, by performing calibration curve fits using both the upper and lower error bounds of the calibration points and comparing the resulting flux differences between these two cases, the uncertainty in the energy scale is determined. The corresponding flux uncertainty is estimated to be 4.6%.

The uncertainty in the reconstructed saturated event energy affects the count numbers in different energy bins. Its impact on the flux uncertainty is realized by affecting the best-fit value (k in the next section). To estimate this conservatively, we construct two energy spectra: the first based on the reconstructed energy plus the upper error, and the second on the reconstructed energy minus the lower error. By comparing the flux differences between these two distributions, we estimate the uncertainty in the reconstructed energy and the corresponding fluxes uncertainty is estimated to be 5.1%.

Systematic uncertainties from material dimensions are quantified through simulation. For example, a 0.2 cm uncertainty in the quartz glass vessel radius contributes 1.2% to the muon flux uncertainty, calculated as the relative change in reconstructed muon events when the radius varies by ± 0.2 cm. Finally, the total uncertainty of muon flux, muon-induced electron flux, and muon-induced neutron flux, derived through error propagation, are calculated as 7.0%, 7.1%, and 7.2%, respectively.

Flux Measurements of Muons, Muon-Induced Electrons, and Muon-Induced Neutrons

It is assumed that the energy spectrum of cosmic-ray muons in the detector comprises contributions from three distinct components: muons, muon-induced electrons, and muon-induced neutron recoils. By employing simulated energy distributions of the detector, we can fit the energy distribution of experimental data points to derive both the spectral composition and flux in the measured spectrum. This fitting procedure is mathematically expressed as:

$$f(E_{\text{data}}) = k \times f(E_{\text{sim}})$$

where k denotes the best-fit value, and f(E_sim) represents a step function approximation of the simulated energy distribution, constructed using 20 equal-width bins.

The left panel of Fig. 10 shows the measured energy spectrum of the detector. The ^{2}/n.d.f. of this fit is calculated to be 8.25/11 under the binning shown in the figure. k is determined to be 1.03 ± 0.19, where the uncertainty is dominated by the statistics of data. The right panel of Fig. 10 displays neutron and alpha recoil events. Data in the energy region below 10 MeVee are derived from prior studies and spontaneous fission of the ^{23} U had been considered [16,19]. Data above 10 MeVee originate from neutron recoil events selected via n- discrimination applied to reconstructed saturated events. Uncertainties are calculated using Poisson statistics at the 90% confidence level. In addition, the pink area in the figure represents the energy spectrum of the recoil protons after calculating the quenching effect in the simulation, which comes from neutrons entering from outside the detector.

Furthermore, since muon-induced electrons and neutrons originate externally to the detector, the fluxes of muon, muon-induced electron, and muon-induced neutron can be expressed as:

$$\phi_{\mu,e} = k \times \sum_{i} f(E_i^{\mu,e}) \times W_i$$

$$\phi_{n} = k \times \sum_{i=1}^{\text{bins}} f(E_i) \times W_i$$

where bins represents the i-th energy bin, f(E_i^) represents the flux value of muons in the i-th bin, W_i is their width and W_i = 5 MeV. Therefore, the total flux can be calculated as the sum of flux values within all bins. The fluxes are calculated as:

$$\phi_{\mu} = (3.64 \pm 0.69_{\text{stat}} \pm 0.25_{\text{syst}}) \times 10^{-10}\text{cm}^{-2}\text{s}^{-1}$$

$$\phi_e = (5.59 \pm 1.06_{\text{stat}} \pm 0.40_{\text{syst}}) \times 10^{-10}\text{cm}^{-2}\text{s}^{-1}$$

$$\phi_n = (6.92 \pm 1.31_{\text{stat}} \pm 0.50_{\text{syst}}) \times 10^{-12}\text{cm}^{-2}\text{s}^{-1}$$

The calculated muon-induced electron flux exceeds the muon event flux, as a single muon traversing material generates multiple electrons along its path, with 93.2% of these electron events exhibiting energy depositions below 10 MeVee. For proton recoil events caused by muon-induced neutrons, after considering the quenching effect, 7.9% of the events are distributed above 10 MeVee. This shows that the flux results above 10 MeVee are below the detector's measurement threshold (1 count per 412 days). Additionally, measurements at CJPL indicate that the neutron yield from muons passing through LS is approximately 0.028 per muon [42]. Therefore, no muon-induced neutron events above 10 MeVee were detected in the 412 day measurement results. At the 90% Poisson confidence level, the upper limit for such events above 10 MeVee is 2.3 counts, corresponding to a flux upper limit of 3.52 × 10 cm ² s ¹.

SUMMARY

In this study, we measured the muon flux, muon-induced neutron flux, and muon-induced electron flux inside the PE room of the CJPL Underground Laboratory using a 28L Gd-LS detector. For saturated signals exceeding the dynamic range of the DAQ system, we reconstructed the charge integration Q-values via a function-fitting method, with the maximum deviation in reconstruction calculated to be below 10%. Geant4 simulation software was employed for detector efficiency estimation and energy calibration curve correction. The measured muon flux was determined as (3.64 ± 0.69_stat ± 0.25_syst) × 10 ¹ cm ² s ¹, the upper limit of the muon-induced neutron flux at the 90% confidence level is 3.52 × 10 cm ² s ¹, and the muon-induced electron flux is (5.59 ± 1.06_stat ± 0.40_syst) × 10 ¹ cm ² s ¹. The measurement results indicate that the cosmic-ray flux at CJPL is at an exceptionally low level, with the flux of muon-induced neutrons being an order of magnitude lower than that of muons. Therefore, the contribution of muon-induced neutrons in the entire laboratory can be neglected.

BIBLIOGRAPHY

[1] W. P. Liu, Z. H. Li, J. J. he, et al., Progress of Underground Nuclear Astrophysics Experiment JUNA in China, Nuclear Physics News, 63: 43 (2022). DOI: 10.1007/s00601-022-01730-0

[2] Q. Yue, W. Zhao, K. J. Kang, et al., Limits on light WIMPs from the CDEX-1 experiment with a p-type point-contact germanium detector at the China Jingping Underground Laboratory, Phys. Rev. D, 90: 091701 (2014). DOI: 10.1103/PhysRevD.90.091701

[3] Y. Bai, Dark matter is darker, Nuclear Science and Techniques, 6: 34 (2023). DOI: 10.1007/S41365-023-01249-5
[4] GERDA Collaboration, GERDA results and the future perspectives for the neutrinoless double beta decay search using Ge, Int. J. Mod. Phys. A, 33: 1843004 (2018). DOI: 10.1142/S0217751X18430042
[5] Stefano Dell' Oro, Simone Marcocci, Matteo Viel, et al., Neutrinoless Double Beta Decay: 2015 Review, Adv. High Energy Phys, 2016: 2162659 (2016). DOI: 10.1155/2016/2162659
[6] Bhaskar Dutta, Wei Chih Huang, Doojin Kim, et al., Prospects for Light Dark Matter Searches at Large-Volume Neutrino Detectors, Phys. Rep, 133: 161801 (2024). DOI: 10.1103/PhysRevLett.133.161801
[7] Y. L. Yan, W. X. Zhong, S. T. Lin, et al., Study on cosmogenic radioactive production in germanium as a background for future rare event search experiments, Nuclear Science and Techniques, 31: 55 (2020). DOI: 10.1007/s41365-020-00762-1
[8] G. Bertone, The moment of truth for WIMP Dark Matter, Nature, 468: 389-393 (2010). DOI: 10.1038/nature09509
[9] M. Auger, D. J. Auty, P. S. Barbeau, et al., Search for Neutrinoless Double-Beta Decay in ^{13} Xe with EXO-200, Phys. Rev. Lett. 109: 032505 (2012). DOI: 10.1103/PhysRevLett.109.032505
[10] J. P. Cheng, K. J. Kang, J. M. Li, et al., The China Jinping underground laboratory and its early science, Annu Rev Nucl Part Sci, 67: 231 (2017). DOI: 10.1146/annurev-nucl-102115-044702
[11] K. J. Kang, J. P. Cheng, Y. H. Chen, et al., Status and prospects of a deep underground laboratory in China, Phys.: Conf. Ser, 203: 012028 (2010). DOI: 10.1088/1742-6596/203/1/012028
[12] B. Aharmim, S. N. Ahmed, T. C. Andersen, et al., Measurement of the cosmic ray and neutrino-induced muon flux at the Sudbury neutrino observatory, Phys. Rev. D, 80: 012001 (2009). DOI: 10.1103/PhysRevD.80.012001
[13] Y. C. Wu, X. Q. Hao, Q. Yue, et al., Measurement of cosmic ray flux in the China JinPing underground laboratory, Chinese Physics C, 37: 086001 (2013). DOI: 10.1088/1674-1137/37/8/086001
[14] Z. Y. Guo, Lars Bathe Peters1, S. M. Chen, et al., Muon flux measurement at China Jinping Underground Laboratory, Chinese Physics C, 45: 025001 (2021). DOI: 10.1088/1674-1137/abccae
[15] V. A. Kudryavtsev, L. Pandola and V. Tomasello, Neutron- and muon-induced background in underground physics experiments, Eur. Phys. J, 36: 171 (2008). DOI: 10.1140/epja/i2007-10472-4
[16] Q. Du, S. T. Lin, S. K. Liu, , et al., Measurement of the fast neutron background at the China Jinping Underground Laboratory, Instrum. Meth. A, 889: 105-112 (2018). DOI: 10.1016/j.nima.2018.01.098
[17] M. B. Gromov, D. S. Kuznetsov, A. E. Murchenko, et al., Stability of Gadolinium-Doped Liquid Organic Scintillators, Technical Physics Letters, 44: 251-254 (2018). DOI: 10.1134/S1063785018030185
[18] Q. Du, S. T. Lin, H. T. He, et al., Response of gadolinium doped liquid scintillator to charged particles: measurement based on intrinsic U/Th contam-

ination, JINST, 13: P04001 (2018). DOI: 10.1088/1748-0221/13/04/P04001
[19] W. X. Zhong, C. H. Fang, S. T. Lin, et al., Identification of neutron sources and background levels in the polyethylene room of the China Jinping Underground Laboratory, JINST, 16: P12003 (2021). DOI: 10.1088/1748-0221/16/12/P12003
[20] S. X. Liu, W. Zhang, Z. H. Zhang, et al., Performance of real-time neutron/gamma discrimination methods, Nuclear Science and Techniques, 34: 8 (2023). DOI: 10.1007/s41365-023-01306-6
[21] H. L. Ran, M. L. Zhe, Y. X. Long, et al., Discrimination of neutron and gamma ray using the ladder gradient method and analysis of filter adaptability, Nuclear Science and Techniques, 12: 33 (2022). DOI: 10.1007/S41365-022-01136-5
[22] J. X. Li, H. L. Hou, Y. F. Huang, et al., Pulse-shaping method for real-time neutron/gamma discrimination at low sampling rates, Nuclear Science and Techniques, 34: 165 (2023). DOI: 10.1007/s41365-023-01306-z
[23] Z. M. Zeng, H. Gong, Q. Yue, et al., Thermal neutron background measurement in CJPL, Nucl. Instrum. Meth. A, 804: 108 (2015). DOI: 10.1016/j.nima.2015.09.043
[24] Y. W. Hu, H. Y. Jiang, Z. Q. Cui, et al., Simulation method for measurement of the cross-section of the ^{1}N(n,)^{11}B reaction using a gridded ionization chamber, Nuclear Science and Techniques, 32: 78 (2021). DOI: 10.1007/s41365-021-00921-y
[25] Y. T. Li, W. P. Lin, B. S. Gao, et al., Development of a low-background neutron detector array, Nuclear Science and Techniques, 33: 41 (2022). DOI: 10.1007/s41365-022-01030-0
[26] Q. Xiao, J. H. Cheng, Y. Y. Xu, et al., Decay in extreme laser fields within a deformed Gamow-like model, Nuclear Science and Techniques, 35: 27 (2024). DOI: 10.1007/s41365-024-01371-y
[27] Dejan Jokovic, Dimitrije Maletic, Aleksandar Dragic, et al., Application of Geant4 simulation in measurement of cosmic-ray muon flux and studies of muon-induced background, Eur. Phys. J. Plus, 138: 1006 (2023). DOI: 10.1140/epjp/s13360-023-04638-0
[28] L. X. Zhang, S. Z. Chen, Z. D. Zhang, et al., Resolution analysis of thermal neutron radiography based on accelerator-driven compact neutron source, Nuclear Science and Techniques, 34: 76 (2023). DOI: 10.1007/s41365-023-01227-x
[29] H. Park, J. Kim, Y. Hwang, et al., Neutron spectrum at the underground laboratory for the ultra low background experiment, Appl. Radiat. Isot, 81: 302-306 (2013). DOI: 10.1016/j.apradiso.2013.03.068
[30] J. M. Xue, S. Feng, Y. H, Chen, et al., Measurement of the neutron-induced total cross sections of natPb from 0.3 eV to 20 MeV on the Back-n at CSNS. Nuclear Science and Techniques, 35: 18 (2024). DOI: 10.1007/s41365-024-01370-z
[31] Q. Zhang, Y. Ge, Y. L. Li, Source-less density measurement using an adaptive neutron-induced gamma correction method, Nuclear Science and Techniques, 34: 125 (2023). DOI: 10.1007/s41365-023-01274-4
[32] W. Tang, J. G. Liang, Y. Ge, et al., A method for neutron-induced gamma

spectra decomposition analysis based on Geant4 simulation, Nuclear Science and Techniques, 33: 154 (2022). DOI: 10.1007/s41365-022-01144-5
[33] Bhaskar Mukherjee, A novel neutron energy spectrum unfolding tool using a genetic algorithm, Nucl. Instrum. Meth. A, 432: 305 (1999). DOI: 10.1016/S0168-9002(99)00535-5
[34] W. Chen, L. Ma, J. H. Chen, et al., Gamma-, neutron-, and muon-induced environmental background simulations for [1] Mo-based bolometric double-beta decay experiment at Jinping Underground Laboratory, Nuclear Science and Techniques, 34: 135 (2023). DOI: 10.1007/s41365-023-01299-9
[35] Y. Xu, Y. S. Ning, Z. Z. Qin, et al., Development of a scintillating-fiber-based beam monitor the coherent muon-to-electron transition experiment, Nuclear Science and Techniques, 35: 79 (2024). DOI: 10.1007/s41365-024-01442-0
[36] A. Bettini, Underground laboratories, Nuclear Instruments and Methods in Physics Research A, 626-627: S64-S68 (2011). DOI: 10.1016/j.nima.2010.05.017
[37] GEANT4 collaboration, GEANT4-a simulation toolkit, Nucl. Instrum. Meth. A, 506: 250-303 (2003). DOI: 10.1016/S0168-9002(03)01368-8
[38] W. W. Wei, Q. Du, L. Wang, et al., Manufacture of gadolinium-doped liquid scintillator detector, High Power Laser and Particle Beams, 27: 066001 (2015). DOI: 10.11884/HPLPB201527.066001
[39] Q. D. Hu, H. Ma, Z. Zeng, et al., Neutron background measurements at China Jinping underground laboratory with a Bonner multi-sphere spectrometer, Nucl. Instrum. Meth. A, 859: 37-40 (2017). DOI: 10.1016/j.nima.2017.03.048
[40] Y. Liu, J. J. Zhu, Neil Roberts, et al., Recovery of saturated signal waveform acquired from high-energy particles with artificial neural networks, Nuclear Science and Techniques, 30: 30 (2019). DOI: 10.1007/s41365-019-0677-0
[41] B. Mahmoodzadeh Vaziri, A. Shahsavand, Analysis of supersonic separators geometry using generalized radial basis function (GRBF) artificial neural networks, Nucl. Instrum. Meth. A, 13: 30-41 (2013). DOI: 10.1016/j.jngse.2013.03.004
[42] X. S. Zhang, J. J. Li, S. M. Chen, et al., Study of neutron production for 360 GeV cosmic muons, Phys.Rev.D, 110: 112017 (2024). https://doi.org/10.1103/PhysRevD.110.112017

Figures

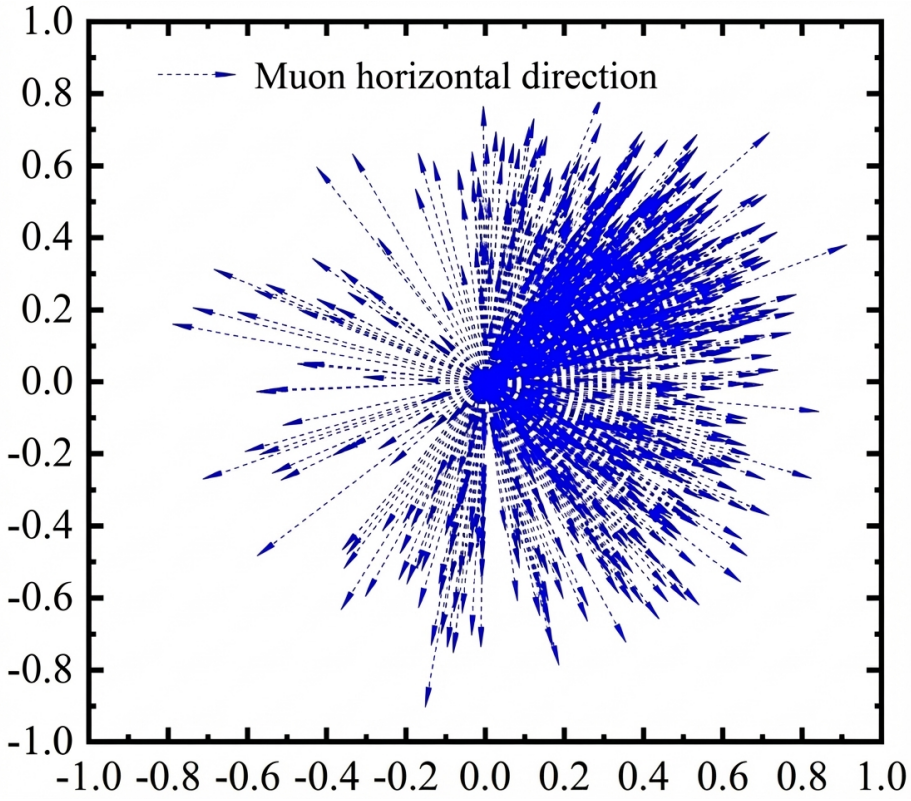

Figure 1: Figure 9

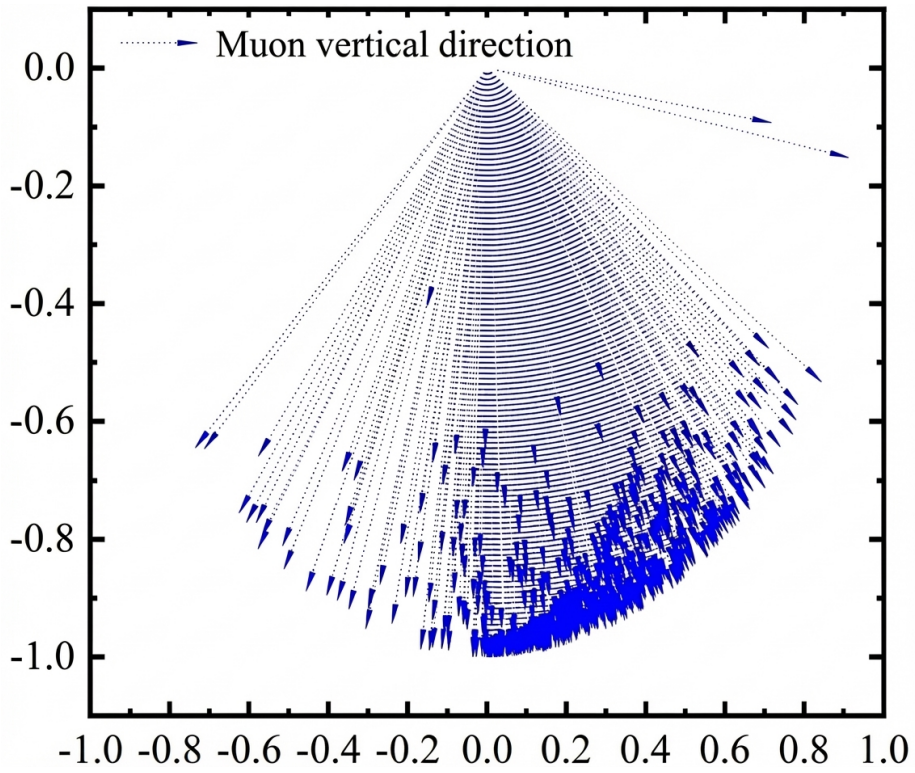

Figure 2: Figure 11